Novel methods to study sea ice deformation, linear kinematic features and coherent dynamic elements from imaging remote sensing data

Polona Itkin[1]

[1]UiT The Arctic University of Norway

Correspondence: Polona Itkin (polona.itkin@uit.no)

Abstract. Satellite Synthetic Aperture Radar (SAR) data are commonly utilized for calculating sea ice displacements and, consequently, sea ice deformation strain rates. However, strain rate calculations often suffer from a poor signal-to-noise ratio, especially for products with a spatial resolution higher than 1 km. In this study, we applied a new filtering method to strain rate calculations derived from Sentinel-1 SAR image pairs with a spatial resolution of 800 m. Subsequently, we employed a

5 power law to evaluate the deformation rates at decreasing spatial resolutions, assessing the quality of the filtered data. Upon positive evaluation of the filtered data, we introduced two innovative methods for sea ice deformation assessment. The first method, named 'damage parcels' (DP) tracking, involved the combined analysis of displacements and deformation strain rates to monitor divergence and convergence within the sea ice cover. Additionally, we proposed a new term to describe the behavior of the winter pack: 'Coherent Dynamic Elements' (CDE). CDEs are cohesive clusters of ice plates within the pack ice that

10 move coherently along Linear Kinematic Features (LKFs). The second novel method developed in this study focused on exploring the geometrical properties of these CDEs. Both methods were applied to the winter collection of Sentinel-1 SAR imagery available during the N-ICE2015 campaign. Our results revealed a cyclically changing winter sea ice cover, marked by synoptic events and transitions from pack ice to the marginal ice zone. The DP were continuously tracked over a period of three weeks, including a major storm, revealing a remarkably slow healing process of existing LKFs. Furthermore, the CDE

15 analysis demonstrated the presence of elongated CDEs with a density ranging from 5 to 20 per 100 km by 100 km, and the shortest distance between LKFs was found to be 5-10 km.

1 Introduction

Sea ice deformation has wide-ranging implications for climate, biology, and navigation. With the Arctic ice thinning, becom-

20 ing more seasonal, and increasing in mobility (Meredith and Schuur, 2019), the processes of sea ice deformation are likely intensifying (Rampal et al., 2009; Olason and Notz, 2014; Itkin et al., 2017). This escalation in sea ice deformation is poised to erode the long-term memory of sea ice thickness and diminish seasonal predictability (Serreze and Meier, 2019; Bushuk et al.,

2020). Deformation, through dynamical thickening and surface roughening (Kwok and Cunningham, 2015; Itkin et al., 2018; von Albedyll et al., 2022), also significantly influences the initial state of sea ice, critical for accurate sea ice forecasting and projections (Bushuk et al., 2017; Tian et al., 2021). To monitor sea ice states and developments, numerical models and satellite remote sensing products are indispensable tools. However, existing sea ice rheologies in numerical models, such as those by Hibler (1979), Hunke and Dukowicz (1997), Heorton et al. (2018) and Ólason et al. (2022), do not entirely align with satellite-derived kinematic properties (Hutter et al., 2022). Furthermore, reliable detection of deformed ice and leads (Zakhvatkina et al., 2019; Lohse et al., 2020; Guo et al., 2023), sea ice roughness (Farrell et al., 2020), and sea ice thickness (Ricker et al., 2017) through satellite remote sensing techniques remains challenging and is plagued by significant uncertainties (Zygmuntowska et al., 2014; Landy et al., 2020).

Decades of research on sea ice deformation have yielded significant progress, leading to a deep understanding of its multi-fractal nature, as extensively documented in the literature (Erlingsson, 1988; Schulson, 2004; Marsan et al., 2004; Hutchings et al., 2011; Itkin et al., 2017; Oikkonen et al., 2017). This body of knowledge reveals that various features, such as small cracks approximately 1 m wide, ridges with a width of 10 m, leads spanning 100 m or more, and even complex systems of Linear Kinematic Features (LKFs) measuring 1 km or wider, exhibit similar characteristics in both space and time. This self-similarity extends not only to their shapes but also to the strain rates within these fractures. Such patterns can be described using scaling laws, enabling the measurement of deformation at a specific spatial or temporal resolution and facilitating comparisons between different datasets, regions, and seasons. These comparisons, in turn, are instrumental for evaluating numerical models (Rampal et al., 2019; Hutter et al., 2022). Furthermore, it has been observed that sea ice fractures of various spatial scales tend to occur at typical intersection angles (Erlingsson, 1988; Hutter et al., 2022; Ringeisen et al., 2023). These fractures connect to form individual ice plates that move relative to each other, resembling the motion of plates in planetary plate tectonics (Erlingsson, 1988; Schulson, 2004). Motion along these fractures can persist for several days (Coon et al., 2007; Graham et al., 2019), although strain rates typically cycle between divergence and convergence over the course of a weather event (Graham et al., 2019).

Although deformation can be estimated from buoy positions and velocities (Rampal et al., 2009; Hutchings et al., 2011; Itkin et al., 2017) or obtaining displacements by comparing images, such as those from X-band ship radar (Oikkonen et al., 2017), much of the progress in this field is reliant on a vast volume of C-band satellite Synthetic Aperture Radar (SAR) data, including missions such as RADARSAT-1 (Kwok, 1998), RADARSAT-2 (Kwok and Cunningham, 2015), and Sentinel-1 (Ringeisen et al., 2023). Sea ice drift can be determined from displacements in SAR images using feature or pattern tracking algorithms (Hollands and Dierking, 2011; Komarov and Barber, 2014; Korosov and Rampal, 2017), which are then utilized to calculate strain rates (Kwok, 1998; Kwok and Cunningham, 2015; von Albedyll et al., 2021). Specifically, the RADARSAT Geophysical Processor System (RGPS) (Kwok, 1998) has been instrumental in deriving scaling laws (Marsan et al., 2004; Bouillon and Rampal, 2015; Rampal et al., 2019) and intersection angles (Hutter et al., 2022). However, the spatial resolution has been constrained to coarser than 1 km due to low signal-to-noise ratio (von Albedyll et al., 2021; Ringeisen et al., 2023). The aim of this paper is to explore the potential use of Sentinel-1 SAR data at higher spatial resolutions to investigate sea ice deformation properties. Specifically, this study will examine if SAR data can be employed to track damage along fractures

between temporally separate weather events. Furthermore, the paper will explore the possibility of detecting the boundaries of rigid ice plates, referred to as 'Coherent Dynamic Elements' (CDE), that move coherently along these fractures.

60 This paper utilizes sea ice deformation data and findings from the N-ICE2015 expedition conducted in January and February 2015 in the pack ice north of Svalbard, as reported by (Granskog et al., 2018), Itkin et al. (2017), Oikkonen et al. (2017) and Graham et al. (2019). The primary objective is to develop and test Sentinel-1 SAR sea ice deformation methods based on the N-ICE2015 dataset. The methodology involves comparing the power law of SAR-derived strain rates with other N-ICE2015 data, tracking 'damage parcels' using SAR-derived data, and calculating CDEs and their associated statistics. The results are
65 shortly discussed for each of these methods in the 'Results and Discussion' subsections.

2 Data

The N-ICE2015 expedition (Granskog et al., 2018), conducted aboard RV Lance as it drifted freely with the pack ice, provided an exceptional dataset on sea ice deformation. This expedition marked a historic moment as it enabled simultaneous high-resolution deformation observations from GPS buoys (Itkin et al., 2015), ship radar (Haapala et al., 2017), and satellite
70 Synthetic Aperture Radar (SAR). In this paper, data from the winter leg (leg 1) spanning from mid-January to mid-February was utilized. During this period, the pack ice in the N-ICE2015 region consisted mainly of second-year ice (SYI) to the north and northwest of RV Lance, while first-year ice (FYI) was prevalent in the south and southeast (Itkin et al., 2017). Over the course of the month analyzed in this study, the distance between the ship and the ice edge decreased from 200 km to 50 km. Additionally, several storms, which induced significant sea ice deformation, passed over the pack ice during this timeframe
75 (Graham et al., 2019). For a comprehensive understanding of sea ice deformation during N-ICE2015, readers are encouraged to refer to the works of Itkin et al. (2017) and Oikkonen et al. (2017). Further details regarding the expedition's atmosphere-ice-ocean interactions can be found in the summary provided by Graham et al. (2019).

Central to this paper are the 145 Sentinel-1A Synthetic Aperture Radar (SAR) images obtained from the CREODIAS 2.0 server (cre, 2023), tracking the same sea ice area during the N-ICE2015 expedition north of Svalbard from 15 January to 18
80 February 2015. An additional 49 images were downloaded to extend the Coherent Dynamic Elements (CDE) analysis until 27 February. These images were among the initial operational data from the European Space Agency's (ESA) Sentinel-1A mission. All the satellite images were acquired in Extra Wide Swath (EW) mode, the typical mode activated over sea ice, providing Level-1 Ground Range Detected (GRD) images with a 410 km wide swath and a pixel size of 40 m by 40 m. The advantageous high latitude location of the expedition allowed for data collection in two temporal clusters of the polar-orbiting
85 satellite: the ascending orbit in the early morning (5 to 8 UTC) and the descending orbit in the afternoon (13 to 16 UTC). However, there were several episodes during the month when GRD data were unavailable, notably between 27 January and 3 February. For this study, information from individual images was processed into displacements, drift, and deformation. These data were then tiled, as described in the 'SAR Sea Ice Deformation Processing' section under the 'Methods' section.

The ship radar data from N-ICE2015 were obtained through the digitizing unit of the navigational X-band radar installed on
90 RV Lance Karvonen (2016); Haapala et al. (2017). The radar antenna, positioned at a considerable height on the ship's mast,

offered a range of 15 km with minimal mast shading and a spatial resolution of 12.5 m. For this study, the processed total deformation rates derived from daily radar image pairs, as processed by Oikkonen et al. (2017), were utilized. To align with the temporal coverage of the Sentinel-1 data, the week between 27 January and 3 February was excluded for comparative analysis.

During the N-ICE2015 expedition, an extensive array of GPS buoys was deployed in two concentric rings around RV Lance, transmitting data at hourly and 3-hourly intervals (Itkin et al., 2015). For this study, only the inner ring, with a diameter of approximately 20 km and comprising 11 buoys, was analyzed. The external ring of buoys was incomplete towards the north and thus excluded from the analysis.

3 Methods

All datasets were processed into spatially distributed points, capturing known displacements at defined, ideally daily, timesteps. The highest spatial scales of the ship radar and buoy data were determined based on signal-to-noise ratios, following the approach suggested by Hutchings et al. (2012). For more detailed information on the processing of ship radar and buoy data, readers can refer to Oikkonen et al. (2017) and Itkin et al. (2017).

The SAR-derived displacements underwent quality control procedures in accordance with Korosov and Rampal (2017). Further details on this quality control process are provided in the following section.

The estimation of sea ice deformation from sea ice displacements followed the same method for all three datasets. Initially, the displacement location points were triangulated using Delaunay triangulation, where triangles with one of the angles sharper than 15 degrees were discarded. Sea ice deformation was then estimated using the commonly-used line integrals of Green's theorem (Marsan et al., 2004; Hutchings and Hibler III, 2008). Shear and divergence were estimated from spatial derivatives of displacements: u_x, u_y, v_x and v_y. u_x is defined as:

$$u_x = \frac{1}{A}\Sigma_{i=1}^n (u_{i+1} + u_i)(y_{i+1} - y_i) \tag{1}$$

, where A is is the area of triangle, i is the index of a corner of triangle, $n = 3$ and $n + 1 = 1$. The other derivatives are defined in a similar way. Then the shear ϵ_{SHR}, divergence ϵ_{DIV} and total deformation rate ϵ_{TOT} are defined as:

$$\epsilon_{SHR} = \sqrt{(u_x - v_y)^2 + (u_y + v_x)^2} \tag{2}$$

,

$$\epsilon_{DIV} = u_x + v_y \tag{3}$$

,

$$\epsilon_{TOT} = \sqrt{\epsilon_{DIV}^2 + \epsilon_{SHR}^2} \tag{4}$$

4

.

3.1 SAR sea ice deformation processing

120 Sea ice displacements from SAR image pairs were estimated using a sequence of feature tracking (FT) and pattern matching (PM) methods developed by Korosov and Rampal (2017). Initially, each image was multi-looked, averaging radar intensity values over an 80 m by 80 m area. This process helped mitigate speckle noise that could introduce errors in the geographical positioning of features or patterns in the image. In the subsequent step, the FT method provided the initial estimate of displacements on an irregular grid for each SAR image pair. These initial estimates were used to narrow the local search ra-

125 dius, improving the computational efficiency of the subsequent PM method applied to the same image pair. For PM, a regular orthogonal grid with points separated by 800 m (10 pixels) was seeded. Using a regular grid was advantageous for sea ice deformation calculations as it provided the foundation for a triangulation mesh with elements of comparable length scales. In the PM method, image sub-samples (templates) measuring 3.2 km by 3.2 km (45 by 45 pixels) were matched based on mean displacements from FT. Maximum cross-correlation (MCC) with rotation was utilized to estimate displacements, and

130 a threshold value of the Hessian matrix of the MCC was empirically determined and employed as a quality control measure. Displacements with values lower than this threshold were discarded, effectively removing geometrical artifacts such as image edges. The remaining displacements were then converted into average velocities by dividing them by the time differences between the images in the pair. Finally, the positions and velocities of the grid points were used to estimate sea ice deformation, following the procedure described in the previous section.

135 In this study, an 800 m distance between grid points was chosen as the highest resolution for the SAR data analysis. Although a higher resolution was technically feasible, it would not be advantageous for the comparison with the ship radar and buoy data. The 800 m grid spacing aligns with one of the shorter length scales of ship radar data and is wider than most of the leads and Linear Kinematic Features (LKFs) observed during N-ICE2015, as reported by Graham et al. (2019). Opting for a shorter distance would have limited the sampling of the shortest distance (λ) over these fracture zones, compromising the accuracy of

140 the power law scaling analysis.

The accuracy of the data, denoted as σ_x, can be estimated as 80 m, representing the lowest detectable displacement. Following the noise-signal ratio formulation by Hutchings et al. (2012), sea ice deformation calculations become reasonably noise-free when $A >> 8n^2\sigma_x^2$, where A is the area of the polygon with n-number of nodes (3 nodes for a triangle). If $\lambda = \sqrt{A}$, this condition is satisfied only when $\lambda >> 679$ m, which corresponds to scales approximately 10 km. Consequently, sea ice

145 deformation calculations at shorter length scales are not reliable. This limitation is clearly visible in Figure 3. The noise arises from undetectable displacements shorter than the pixel size (σ_x) of the SAR images. These short displacements are extremely low or even close to zero. The residual deformation resulting from these displacements accumulates in artifacts with rhomboid shapes. These shapes appear due to the step function in the sea ice drift algorithm: the value of a displacement can only increase by σ_x. These increases occur perpendicular and parallel to the template rotation in PM, creating a rhomboid pattern that

150 becomes denser in regions where the velocity gradients are larger. It's crucial to note that this pattern should not be confused with similarly-shaped fractures following Mohr-Coulomb failure lines in Linear Kinematic Features (LKFs) (Erlingsson, 1988;

5

Schulson, 2004; Dansereau et al., 2019). Realistic features, however, stand out as locations with a stronger signal, correctly spatially confined to leads (see Figure 2). Calculating deformation at a coarser spatial resolution, which would smooth the rhomboid artifacts, would inevitably lead to the loss of information about the location of deforming sea ice. As demonstrated by Korosov and Rampal (2017) using the example of coastline locations, the sea ice drift algorithm exhibited a spatial accuracy of approximately 200 m, significantly higher than the 800 m resolution used in this study.

To examine if also the deformation values in those features were realistic they were isolated by applying a detection limit DL defined as:

$$DL = nk\sigma_x^2/(2Adt), \tag{5}$$

where k is the scaling coefficient of σ_x, and dt is the time difference between the images in the image pair. The rhomboid artifacts have values right at the DL for $k = 1$ and can be efficiently removed by threshold DL for e.g. $k = 1.3$. In this study this increases the σ_x for 30% from 80 m to approximately 120 m.

In addition to the noise-signal ratio issues in the displacement data, another source of error in the deformation estimates by line integrals stems from the orientation of the Linear Kinematic Features (LKFs) concerning the triangle boundaries. Equation 1 assumes a homogeneous velocity gradient along the boundary, a condition often violated in triangles - polygons with just three nodes, where an LKF can cross its boundary under any angle. This 'boundary-definition error' is a well-known problem (**??**) that can lead to spurious opening and closing along the LKFs. While this problem can be mitigated by spatial smoothing (**?**), Bouillon and Rampal (2015) suggested a directional filtering of deformation values of triangles specifically along the LKFs. Such a filter, known as the LKF filter (LKFF), was applied in this study to the data previously filtered by DLDL. The suggested kernel size of 3 triangles (Bouillon and Rampal, 2015) was used, along with an additional criterion: only deformation features with at least one entire kernel size were considered, while the others were removed. Some of the rhomboid artifacts persisted after the DLDL filtering, owing to accumulated noise in the 'corners' of the rhomboids, where two directions of the step function crossed. The additional criterion, specifying the minimal LKF size, helped eliminate such artifacts. LKFF averages out the spurious switching between divergence and convergence from one triangle to the next (see Figure 3) and reduces the deformation values. As triangles along the LKFs may have varying sizes, the averages were weighted by the triangle area.

The overview of the methods for SAR sea ice deformation used in this paper is given in Figure 4.

Each SAR image pair had a restricted spatial extent and occasionally did not cover the entire sea ice surface. To expand the data coverage, several surrounding image pairs were processed for deformation and then tiled together. Since the time difference between the pairs varied, different DL values were correspondingly applied. Figure 2 already displays such a tiled product.

To facilitate comparison, SAR-derived deformation values were coarse-grained from the original 800 m resolution into logarithmically spaced λ, similar to the other two data sources. The minimum spatial coverage of any coarse-level triangle by

fine triangles was set at 10%, and the assigned values were means weighted by the spatial coverage. Triangles with spatial
coverage below this threshold were discarded.

3.2 Comparison of the N-ICE2015 strain rates

To asses if the sea ice deformation derived from SAR by the methods described in the previous section was realistic, SAR-derived data was compared to the ship radar and buoy data. Unfortunately, were the ship radar and buoy deformation data used in this study just collections of values with no information about their spatial distribution. The ship radar deformation maps calculated by Oikkonen et al. (2017) were not geolocated nor stored and the spatial scales λ of the buoy array are too coarse to compare directly to the ship radar values. To enable the comparison between all three datasets, the power law across all available λ for of daily total deformation ϵ_{TOT} were estimated. Sea ice deformation is known to be a highly localized process, where mean ϵ_{TOT} ($\bar{\epsilon}_{TOT}$) follows the power law with respect to λ: $\bar{\epsilon}_{TOT} = \alpha\lambda^{\beta}$ (Marsan et al., 2004), where α is the interception at $\lambda = 1$ and β is the slope of the power law. The ϵ_{TOT} depends also on the temporal scale at which they were measured - there is a power law also at the increasing temporal scale (Oikkonen et al., 2017). To account for this, the daily resolution of the buoy and ship radar data was strictly observed, while for the SAR image pairs a softer criteria was necessary and only temporal difference between 22 and 26 hours was used for this part of the analysis. The ship radar and buoy data was also filtered by DL values determined by the SAR data. Because the data was collected over the same region and over the same time window, same magnitude of sea ice deformation was expected. This allowed a comparison of α in addition to typically used β (Marsan et al., 2004; Bouillon and Rampal, 2015; Itkin et al., 2017; Oikkonen et al., 2017). The confidence envelope of the power law was estimated as a two-tailed T-test as in Itkin et al. (2017).

3.3 Damage Parcels

The spatially distributed sea ice deformation values obtained in the previous section were used to classify the sea ice cover into damaged (deformed) and undamaged (undeformed) ice. For such classification a zero threshold of total deformation was used. Afterwards, divergence values were used to further classify damaged ice into predominantly ridged (convergence) and predominant lead ice formation (divergence). The advantage of this two-stage classification was that first the total deformation was used to give a relatively reliable division between undamaged and damaged ice. Although the LKFF removed some of the spurious divergence, the second-stage classification was less certain.

Such classification was tracked for a sequence of time steps (SAR image pairs). The second SAR scene in pair was always first scene in the following pair. The strict daily time difference between the image pairs was not observed. The tracking was not done for individual triangles, because of frequent distortion of the triangles beyond the 15 degrees minimal angle criteria. To avoid the numerically costly re-meshing, a simple approach with 'ice parcels' was used instead. Ice parcels can be used in applications where the mass preservation is not critical (e.g. (Liston et al., 2020; Horvath et al., 2023)). Displacements calculated as input to the sea ice deformation calculations were used to update the location of damaged ice parcels was updated between the time steps.

The spatial resolution of the damage parcel product in this study was 800 m, limited by the resolution of the input data (800 m spacing of the sea ice deformation and sea ice displacements), and by the search radius within which the input data is attributed to each parcel (also 800 m). If multiple triangle centroids fell within the search radius, the mean value was attributed to the parcel. If no value was found, the parcel disappeared. New parcels were added in the empty areas between the parcels
220   i.e. wide leads. An early version of this method was used by Guo et al. (2022) for the same study area as in this paper.

3.4   Coherent Dynamic Elements and Linear Kinematic Features

The spatial characteristics of Coherent Dynamic Elements (CDE) and Linear Kinematic Features (LKF) were determined by using the location information of the deformation calculations. The triangle nods filtered by LKFF were used to calculate polygons in computational geometry operations such as union, concave hull, polygon difference (removed intersection) and
225   distance buffering (Figure 5). The concave hull that required to construct the LKF polygons was based on the 'alpha shape' method Edelsbrunner et al. (1983) using Delaunay triangulation and implemented based on Dwyer (2014). Small CDEs are CDEs in the areas enclosed by concave hulls. The resulting polygons were classified into CDEs and LKFs and the following characteristics were determined for each time step:

- CDE density/frequency: number of CDE per total area (km^{-1}). On time steps with very low sea ice deformation the
230   entire region may move homogeneously, while it may divide into many CDEs when the deformation is strong.

- CDE size: area of the CDE (km^2). Similarly to the CDE density, the size of the CDE depends on how strong the deformation between two time steps is.

- CDE fragmentation: circumference divided by mean diameter of CDE, with values close to 0 for perfect circle and > 100 for complex meandering shapes. The latter is typical for CDEs where the LKFF likely fails to detect small deformation
235   and correctly divide the this complex form into several smaller CDEs. Large CDE fragmentation is a measure of error of the method.

- CDE roundness: ratio between max and min diameter of CDE, with values close to 1 for circular CDE.

- LKF fraction: LKF area per total area.

- Distance between LKFs: min and max CDE radius.

240   The vector operations required empirical tuning of parameters such as buffer distances and minimal sizes (Table 1). The buffer distances (buffer and margin buffer) were used to merge disconnected polygons of the same LKFs in cases where parts of it were not detected. Triangulation distance was used as input to the concave hull triangulation. Small values of this distance allow more complex LKF and CDE boundaries. On the contrary, the minimal size of the CDE limited unrealistic fragmentation of ice cover into small CDEs.

Table 1. Empirical parameters used in geometry operations to derive LKF and CDE polygons.

name	description	value in this paper
buffer	Max distance (in m) between two nods of different triangles to get connected into same LKF. This is a circular buffer and there is a trade-off between desirable connecting over parts of a same partly undetected LKF and undesirable connecting across a breath of two separate, but close-by LKFs.	8000
margin buffer	Additional distance (in m) that increases connectivity of LKFs.	3400
triangulation distance	Max distance for Delaunay triangulation (in m) in a concave hull between LKFs. This limits the size of small CDE radius and unrealistically high CDE count.	2000
min area	Min size of the CDE and small CDE (in m^2).	1e6

4 Results and Discussion

4.1 Comparison of the N-ICE2015 strain rates

The spatial power law in ϵ_{TOT} were first compared for the data derived from the N-ICE2015 ship radar and buoys (Figure 6 left). For the full suit of data the power laws have resembling interception, α (20.15 and 15.91) and slope, β (-0.6 ad -0.69). Both power laws extend each other's spatial scales (λ): ship radar from 200 m to 3 km ad buoys from 3 to 8 km. The buoy data power law is based on mean values for only 3 values of λ and has consequently a wide confidence envelope. Before comparison to the filtered SAR-derived data, also the ship radar and buoy data has to be filtered in a similar way (Figure 6 center). Values below DL - estimated from mean DL values in SAR data, were removed from ship radar and buoy data. This increased α and β for ship radar to 24.61 and -0.7, respectively. The removal of values below DL also resulted in slight decrease of α and β to 15.24 and -0.55, respectively. LKFF filtering of the ship radar and buoy data was not possible as described in the Method section under 'Comparison of the N-ICE2015 strain rates'.

The spatial power law in ϵ_{TOT} was initially compared for the data obtained from the N-ICE2015 ship radar and buoys (Figure 6 left). For the complete dataset, the power laws exhibited similar intercepts, α (20.15 and 15.91), and slopes, β (-0.6 and -0.69). Both power laws cover different spatial scales (λ): the ship radar data spans from 200 m to 3 km, while the buoy data ranges from 3 km to 8 km. Before comparing them to the filtered SAR-derived data, the ship radar and buoy data needed to be filtered in a similar manner (Figure 6 center). Values below DL, estimated from mean DL values in SAR data, were removed from the ship radar and buoy data. This filtering increased α and β for ship radar to 24.61 and -0.7, respectively. For the buoys the removal of values below DL led to a counter-intuitive slight decrease in α and β to 15.24 and -0.55, respectively. Note that the the power law for buoy data is based on mean values for only three λ values, resulting in a wider confidence envelope.

LKFF filtering of the ship radar and buoy data was not feasible, as described in the Method section under 'Comparison of the
N-ICE2015 strain rates'.

Figure 6 (center) also shows the power laws for the SAR-derived data. The unfiltered data had a large amount of low values
that decreased the β of the power law. DL filtering successfully removed these values and increased α and β from 4.79 to 14.63
and from -0.14 to -0.59, respectively. To construct the power law, only means for λ shorter than 10 km were used. This will be
revisited later in this section. The LKFF filtering further increased α and β to 18.73 and to -0.73, respectively. The power law
from LKFF-filtered SAR data corresponded well to the ship radar and buoy data power laws within their confidence envelopes.
The temporal resolution is not strictly daily for all datasets, and the area is not strictly the same, so some differences in power
law are expected. Thus, the high deformation rates detected by SAR were reliable, and LKFF SAR-derived deformation was
useful at short λ.

A further confirmation that the LKFF SAR estimates were reliable was the conversion of the ϵ_{TOT} values in Figures 6 (left
and center) to mean total displacements ($\overline{\sigma_x}$). This was done by a simple rearrangement of Equation 5, used to estimate DL,
such that $\overline{\sigma_x} = \sqrt{\frac{\epsilon_{TOT}(2Adt)}{3}}$. The displacements are more intuitive than strain rates and are comparable to any other distances
over space, such as ridge and lead widths or even sea ice thickness. A total displacement of 100 can, for example, mean 70 m
boarding of a lead with 30m of shearing. Figure 6 (right) shows that $\overline{\sigma_x}$ at 1 km were about 200 m for all three datasets. This
corresponded to a triangle with sides of about 1 km experiencing a sum of divergence and shear of approximately 200 m. If
extrapolated to 100 m, $\overline{\sigma_x}$ was approximately 50 m. Both 1 km and 100 m values were within the expected ranges for medium
and small size leads. At 1 m, $\overline{\sigma_x}$ for DL-filtered data were in the range of 3-4 m, and for the non-filtered data for ship radar and
buoy data, it was in the range of 1-2 m. The latter values are comparable to the mean sea ice thickness measured in the pack
ice at N-ICE (Rösel et al., 2018). These values correspond to the expected theoretical values of $\overline{\sigma_x}$ (Weiss, 2017). A practical
use of recalculating the strain rates to total displacement is also in observation (e.g., Nicolaus et al. (2022); Parno et al. (2022))
or simulation design. To resolve, for example, 100 m displacements (small leads), 10 m displacements (large ridges), or 1 m
displacements (cracks), accurate measurements at 200 m, 30 m, or 1 m resolution at daily scale are required.

In addition to the power law of $\overline{\epsilon_{TOT}}$, other values scaled with λ (Figure 6). For example, the DL values followed a power
law which suggested that only at $\lambda \gg 10$ km, no ϵ_{TOT} values fell below DL anymore. This matched the noise-free estimates
following Hutchings et al. (2012) (see the Method section). Finally, another sharp limit stood out in the data: the maximum
values of ϵ_{TOT} and σ_x follow a power law with a matching slope to the DL power law, but with an interception higher by
approximately 2 orders of magnitude. At 1 km, the maximum ϵ_{TOT} and σ_x values were approximately 40 1e-6 s^{-1} and 2 km,
respectively, for all three datasets. There is no natural explanation why σ_x should be limited to values below 2 km, as Arctic
leads and polynyas can be much wider than that (Wernecke and Kaleschke, 2015). This hard limit was a consequence of the
15° angle limit in the triangles used for strain rate calculations and another manifestation of the deficiency of estimates by line
integrals (Green's theorem) (Marsan et al., 2004; Hutchings and Hibler III, 2008) in simple polygons like triangles. The 15°
rule is often violated in fast-deforming features that have relative displacements beyond 2 km over a given time step.

The filtering of SAR-derived deformation resulted in widespread missing values (Figure 7). In the coarse-graining of λ, at
least 10% of the area was required to have valid data. This means that as λ became coarser, data had an increased fraction of

missing values. The problem was demonstrated on maps in Figure 7 with an example from 25 January. The individual LKFs
300   remained visible up to λ 4.5 km. With λ 9.6 km, the lines were discontinued, and only triangles containing either very wide
or multiple LKFs at shorter λ remained. The few remaining values at λ larger than 10 km were relatively high, and their
means did not follow the power law (Figure 6 center). Such a 'breaking point' between 5 and 10 km was previously detected
in the comparison of the hourly buoy and ship radar data from N-ICE2015 (Oikkonen et al., 2017). The reason for it may
reside in the under-detection of the self-similarity of sea ice deformation by the N-ICE2015 data. None of the datasets had a
305   spatial resolution high enough to resolve the cracks. Likewise, all have a spatial extent limited to the local ice cover with a
radius of 10 to 200 km, insufficient to resolve the pan-Arctic systems of LKFs. LKFs remain the only spatial feature which all
three datasets could resolve. Figure 6 showed how removing low values increased the power law slope. Adding values from
unresolved cracks would, therefore, decrease it. Some datasets that could be used to measure deformation cracks (resolution
1-m) already exist (Clemens-Sewall et al., 2022), but have very poor temporal resolution (weekly). On the contrary, adding
310   the spatial extent should decrease the values at large λ to prevent 'the power law breaking'. SAR data are already available at
the pan-Arctic scale (Kwok, 1998; Howell et al., 2022), but the resolution used in this study produces data volumes that are
challenging and will be subject to future studies.

4.2   Damage Parcels

Sea ice damage parcels were tracked for 19 days, starting from 15 January to 3 February (see Figure 8). Daily image pairs were
315   available from 15 January to 27 January. Subsequently, deformation was successfully calculated for an image pair from 27
January to 3 February, allowing the continuation of parcel tracking. During the 8-day period of missing data, from 27 January
to 3 February, the conditions were relatively quiescent in terms of weather and sea ice motion (Itkin et al., 2017; Graham et al.,
2019). Afterward, between 3 February and 5 February, SAR data was available, but the ice cover experienced a major storm
(Graham et al., 2019), leading to unusually strong deformation (Itkin et al., 2017; Graham et al., 2019), which prevented further
320   parcel tracking.

The parcel map (Figure 8) illustrates a network of ice parcels primarily experiencing divergence within LKFs. This pattern
persisted throughout the entire period, with the same parcels undergoing repeated deformation in the form of both divergence
and convergence. Convergence and mixed deformation are localized and confined to narrow belts on the edges of predominantly
diverging ice, a phenomenon observed despite changes in weather conditions and frequent alterations in sea ice drift directions
325   (?). This finding aligns with previous studies (Coon et al., 2007) and indicates that large fractures, where shear and shape
mismatch occurred, healed slowly (Murdza et al., 2022). Recent observational studies on pressure ridges have confirmed
that their keels consolidate over a period of weeks and months (Salganik et al., 2023). The duration of sequential deformation
observed in the damage parcel data can be valuable for constraining the damage-healing behavior of numerical models (Rampal
et al., 2016; Damsgaard et al., 2021; Ólason et al., 2022).
330   Undamaged ice that did not experience any detected deformation did not move uniformly, resulting in variable distances
between individual parcels (Figure 8). Although sea ice parcel classification was based on the filtered sea ice deformation
retrieval, their motion was determined using the unfiltered sea ice displacement. The density of parcels in Figure 8 indicated

undetected deformation with values below the DL. The noise originating from artifacts in the sea ice displacement algorithm was inherently random, and any regular spatial features visible in the ice parcel density were likely a consequence of deformation. For example, in the southern part of the map, there was a continuous curve with increased parcel density, which pointed to real deformation. Under convergence, the relative motion is typically shorter than under divergence and more challenging to detect. As another example, the areas in the southwestern and northeastern corners of the map had sparser parcels, indicating divergence.

4.3 Coherent Dynamic Elements and Linear Kinematic Features

In contrast to the damage parcels, CDE analysis was successfully applied to the sea ice deformation calculations over the entire period from January 15 to February 18. CDE maps (Figure 9 top) showed evolving shapes of the CDEs resembling ice plates seen in optical images (Erlingsson, 1988; Schulson, 2004). These shapes were obtained from daily SAR image pairs as well as those with shorter or longer time differences. The method was also successfully applied in the marginal ice zone (MIZ), albeit not directly at the ice edge to avoid open water areas. The maps displayed a gradient in CDE size, fragmentation, and roundness in the north-south direction from the pack ice towards the MIZ.

Based on the CDE maps, time series of CDE statistics (Figure 9 bottom) were calculated. The time series were extended by 10 days to account for the relocation of RV Lance northwards away from the MIZ (Granskog et al., 2018). The statistics fluctuated around values typical for the quiescent state of the pack ice surrounding RV Lance as it drifted southwards towards the ice edge. The values changed abruptly with each of the three major storms (Graham et al., 2019) that passed the area:

– CDE Density: The CDE density increased from low values below 5 CDEs per 100 by 100 km during quiescent periods to as high as 20 during the storms.

– CDE Area: During the initial quiescent period, the number of CDEs was low, coinciding with a small variability in CDE area, with means just below $20000\pm20000\ km^2$. After the first storm in mid-January, the values decreased by an order of magnitude to $1000\pm1000\ km^2$. The initial high values were never fully restored but increased significantly again only after the relocation of RV Lance away from the MIZ.

– CDE Shape (Roundness): The CDEs were generally not round, as their values were much higher than the theoretical value of 1 for circular forms. Typical values were close to 5, indicating elongated forms with a length five times greater than width. There was a continuous weak increase in CDE roundness during the entire duration of the time series. In comparison, typical roundness values of summer sea ice floes were much higher, with the most frequent value reported as 1.4 and typical values between 1 and 4 (Hwang and Wang, 2022).

– CDE Fragmentation: This measure of under-detected fractures exhibited the largest variability during quiescent periods, reflecting the smallest and most challenging relative motion to detect by SAR. The maps showed that fragmentation was lowest in the MIZ, where distances between the CDEs were largest, and relative motion was high (Figure 9 top).

12

— LKFs Fraction: The lowest LKF fractions, close to 1%, were recorded in mid-January and occasionally increased towards
365   3% during storms. They remained relatively high (2%) in quiescent periods and after the relocation away from the MIZ.

— Distance between LKFs: The maximal and minimal distances between LKFs estimated from CDE diameters were typ-
ically at least 5 to 10 km and at most 50 to 100 km. The highest values were found during quiescent periods and were
lowest during the storms. The distance between the LKFs derived from the CDE perimeters confirmed the findings about
the power law 'breaking,' discussed in the Results and Discussion section under 'Comparison of the N-ICE2015 strain
370   rates.' The lowest distances were between 5 and 10 km, corresponding to the λ breaking point.

Despite the fierceness of the storm in mid-February (Itkin et al., 2017; Graham et al., 2019), the CDE properties at the end of
the time series resembled the ones at the beginning. This pointed to the resilience of the CDEs and their geometrical properties
in the winter pack ice and the potential for healing. However, some properties such as CDE area, roundness, and LKF fraction
never fully recovered to the lowest values recorded in mid-January. Itkin et al. (2017) previously demonstrated an elevated
375   slope of the power law of the N-ICE2015 spring buoy array (April-May 2015) and hypothesized a long-lasting damage to the
sea ice cover caused by this extreme event.

5   Conclusions

This study has successfully demonstrated that Sentinel-1 SAR-derived sea ice deformation data can be effectively utilized at a
spatial resolution of 800 m after mitigating noise generated by sea ice displacement algorithms. This was accomplished through
380   the application of threshold and shape filtering techniques. The accuracy of the SAR-based results was validated against data
from the N-ICE2015 ship radar and buoy observations, utilizing power law properties.

Across spatial scales ranging from 600 m to 5 km, the power law slope and intercept for all three datasets (processed in a
similar manner) were consistently close to 20 and -0.7, respectively. Subsequently, the strain rates were recalculated to obtain
total displacements, revealing a mean total displacement of approximately 200 m at the spatial scale of 1 km.

385   While the power laws of all three datasets exhibited a strong correspondence below 5 km, the SAR-derived power law
'breaks' for the larger spatial scales. This discrepancy was likely attributed to issues related to spatial resolution, wherein
fractures smaller than Linear Kinematic Features (LKFs) are inadequately resolved, coupled with limitations in spatial extent.

The detection of SAR deformation was constrained not only by the lower limit of spatial resolution but also by the minimum
angle of triangles employed in Green's theorem (upper limit).

390   The damage parcels, derived from SAR-based displacements and strain rates, were effectively employed to monitor the
evolution of the sea ice cover over a period of three weeks, encompassing the passage of a major storm and an 8-day data
gap. The temporal stability of the ice pattern was disrupted by an extreme storm in mid-February, as reported by Graham et al.
(2019), after which the tracking of damage parcels became unfeasible.

Up to 20 separate CDEs per area of 100 km by 100 km for each SAR image pair were identified based on the positions
395   of LKFs detected through SAR-derived deformation. During quiescent periods, their typical sizes were 20,000$\pm$20000 km^2,

whereas they reduced to 1,000±1000 km^2 during storms. These CDEs exhibited an elongated shape, with the lowest shape factors (5) resembling the highest shape factors of sea ice floes after breakup, as reported byHwang and Wang (2022). The fraction of the surface area covered by LKFs remained below 3%, and the distances between LKFs varied between 5-10 km and 50-100 km, reflecting minimal and maximal values, respectively.

400   All the methods employed in this study are applicable to both the winter sea ice pack and the MIZ areas. Furthermore, the spatial resolution can be enhanced for Sentinel-1 SAR, and these methods remain adaptable to dense sea ice deformation retrieval from radar or optical imagery, regardless of the data source.

Data availability.

Sentinel-1 SAR data are freely available and were downloaded from CREODIAS (https://creodias.eu/).

405 *Code and data availability.*

The code used in the manuscript is written in Python (with dependence on functions in libraries NumPy, SciPy, PyResample and Shapely) and it is available in the GitHub repository (https://github.com/loniitkina/sid/). The version used to obtain the results of this study will be available at Zenodo at the end of the review process.

Author contributions.

410   PI processed the data, carried out the analysis and wrote the manuscript.

Competing interests.

PI declares that she has no conflict of interest.

References

Copernicus Sentinel data, https://creodias.eu/, 2023.

420 Bouillon, S. and Rampal, P.: On producing sea ice deformation data sets from SAR-derived sea ice motion, The Cryosphere, 9, 663–673, https://doi.org/10.5194/tc-9-663-2015, https://tc.copernicus.org/articles/9/663/2015/, 2015.

Bushuk, M., Msadek, R., Winton, M., Vecchi, G. A., Gudgel, R., Rosati, A., and Yang, X.: Skillful regional prediction of Arctic sea ice on seasonal timescales, Geophysical Research Letters, 44, 4953–4964, https://doi.org/https://doi.org/10.1002/2017GL073155, https://agupubs.onlinelibrary.wiley.com/doi/abs/10.1002/2017GL073155, 2017.

425 Bushuk, M., Winton, M., Bonan, D. B., Blanchard-Wrigglesworth, E., and Delworth, T. L.: A Mechanism for the Arctic Sea Ice Spring Predictability Barrier, Geophysical Research Letters, 47, e2020GL088 335, https://doi.org/https://doi.org/10.1029/2020GL088335, https://agupubs.onlinelibrary.wiley.com/doi/abs/10.1029/2020GL088335, e2020GL088335 10.1029/2020GL088335, 2020.

Clemens-Sewall, D., Polashenski, C., Raphael, I., Perovich, D., and Fons, S.: High-Resolution Repeat Topography of Drifting Ice Floes in the Arctic Ocean from Terrestrial Laser Scanning Collected on the Multidisciplinary drifting Observatory for the Study of Arctic Climate

430 Expedition, https://doi.org/10.18739/A26688K9D, 2022.

Coon, M., Kwok, R., Levy, G., Pruis, M., Schreyer, H., and Sulsky, D.: Arctic Ice Dynamics Joint Experiment (AIDJEX) assumptions revisited and found inadequate, Journal of Geophysical Research: Oceans, 112, https://doi.org/https://doi.org/10.1029/2005JC003393, https://agupubs.onlinelibrary.wiley.com/doi/abs/10.1029/2005JC003393, 2007.

Damsgaard, A., Sergienko, O., and Adcroft, A.: The Effects of Ice Floe-Floe Interactions on Pressure Ridging in Sea Ice, Journal of Advances

435 in Modeling Earth Systems, 13, e2020MS002 336, https://doi.org/https://doi.org/10.1029/2020MS002336, https://agupubs.onlinelibrary.wiley.com/doi/abs/10.1029/2020MS002336, e2020MS002336 2020MS002336, 2021.

Dansereau, V., Démery, V., Berthier, E., Weiss, J., and Ponson, L.: Collective Damage Growth Controls Fault Orientation in Quasibrittle Compressive Failure, Phys. Rev. Lett., 122, 085 501, https://doi.org/10.1103/PhysRevLett.122.085501, https://link.aps.org/doi/10.1103/PhysRevLett.122.085501, 2019.

440 Dwyer, K.: Concave Hulls, https://gist.github.com/dwyerk/10561690, 2014.

Edelsbrunner, H., Kirkpatrick, D., and Seidel, R.: On the shape of a set of points in the plane, IEEE Transactions on Information Theory, 29, 551–559, https://doi.org/10.1109/TIT.1983.1056714, 1983.

Erlingsson, B.: Two-Dimensional Deformation Patterns in Sea Ice, Journal of Glaciology, 34, 301–308, https://doi.org/10.3189/S0022143000007061, 1988.

445 Farrell, S. L., Duncan, K., Buckley, E. M., Richter-Menge, J., and Li, R.: Mapping Sea Ice Surface Topography in High Fidelity With ICESat-2, Geophysical Research Letters, 47, e2020GL090 708, https://doi.org/https://doi.org/10.1029/2020GL090708, https://agupubs.onlinelibrary.wiley.com/doi/abs/10.1029/2020GL090708, e2020GL090708 2020GL090708, 2020.

Graham, R. M., Itkin, P., Meyer, A., Sundfjord, A., Spreen, G., Smedsrud, L. H., Liston, G. E., Cheng, B., Cohen, L., Divine, D., Fer, I., Fransson, A., Gerland, S., Haapala, J., Hudson, S. R., Johansson, A. M., King, J., Merkouriadi, I., Peterson, A. K., Provost, C., Randelhoff,

450 A., Rinke, A., Rösel, A., Sennéchael, N., Walden, V. P., Duarte, P., Assmy, P., Steen, H., and Granskog, M. A.: Winter storms accelerate the demise of sea ice in the Atlantic sector of the Arctic Ocean, Scientific Reports, 9, https://doi.org/10.1038/s41598-019-45574-5, 2019.

Granskog, M. A., Fer, I., Rinke, A., and Steen, H.: Atmosphere-Ice-Ocean-Ecosystem Processes in a Thinner Arctic Sea Ice Regime: The Norwegian Young Sea ICE (N-ICE2015) Expedition, Journal of Geophysical Research: Oceans, 123, 1586–1594, https://doi.org/10.1002/2017JC013328, 2018.

455 Guo, W., Itkin, P., Lohse, J., Johansson, M., and Doulgeris, A. P.: Cross-platform classification of level and deformed sea ice considering per-class incident angle dependency of backscatter intensity, The Cryosphere, 16, 237–257, https://doi.org/10.5194/tc-16-237-2022, https://tc.copernicus.org/articles/16/237/2022/, 2022.

Guo, W., Itkin, P., Singha, S., Doulgeris, A. P., Johansson, M., and Spreen, G.: Sea ice classification of TerraSAR-X ScanSAR images for the MOSAiC expedition incorporating per-class incidence angle dependency of image texture, The Cryosphere, 17, 1279–1297, 460 https://doi.org/10.5194/tc-17-1279-2023, https://tc.copernicus.org/articles/17/1279/2023/, 2023.

Haapala, J., O. A. G. A. I. P. N. M. S. G. L. M. et al.: N-ICE2015 ship radar images [Data set], Norwegian Polar Institute, 10, https://doi.org/https://doi.org/10.21334/npolar.2017.6441ca81, 2017.

Heorton, H. D. B. S., Feltham, D. L., and Tsamados, M.: Stress and deformation characteristics of sea ice in a high-resolution, anisotropic sea ice model, Philosophical Transactions of the Royal Society A: Mathematical, Physical and Engineering Sciences, 376, 20170349, 465 https://doi.org/10.1098/rsta.2017.0349, https://royalsocietypublishing.org/doi/abs/10.1098/rsta.2017.0349, 2018.

Hibler, W. D.: A Dynamic Thermodynamic Sea Ice Model, Journal of Physical Oceanography, 9, 815 – 846, https://doi.org/https://doi.org/10.1175/1520-0485(1979)009<0815:ADTSIM>2.0.CO;2, https://journals.ametsoc.org/view/journals/phoc/9/4/1520-0485_1979_009_0815_adtsim_2_0_co_2.xml, 1979.

Hollands, T. and Dierking, W.: Performance of a multiscale correlation algorithm for the estimation of sea-ice drift from SAR images: initial 470 results, Annals of Glaciology, 52, 311–317, https://doi.org/10.3189/172756411795931462, 2011.

Horvath, S., Boisvert, L., Parker, C., Webster, M., Taylor, P., Boeke, R., Fons, S., and Stewart, J. S.: Database of daily Lagrangian Arctic sea ice parcel drift tracks with coincident ice and atmospheric conditions., Sci Data, 10, https://doi.org/https://doi.org/10.1038/s41597-023-01987-6, https://doi.org/10.1038/s41597-023-01987-6, 2023.

Howell, S. E. L., Brady, M., and Komarov, A. S.: Generating large-scale sea ice motion from Sentinel-1 and the RADARSAT Constella-475 tion Mission using the Environment and Climate Change Canada automated sea ice tracking system, The Cryosphere, 16, 1125–1139, https://doi.org/10.5194/tc-16-1125-2022, https://tc.copernicus.org/articles/16/1125/2022/, 2022.

Hunke, E. C. and Dukowicz, J. K.: An Elastic–Viscous–Plastic Model for Sea Ice Dynamics, Journal of Physical Oceanography, 27, 1849 – 1867, https://doi.org/https://doi.org/10.1175/1520-0485(1997)027<1849:AEVPMF>2.0.CO;2, https://journals.ametsoc.org/view/journals/phoc/27/9/1520-0485_1997_027_1849_aevpmf_2.0.co_2.xml, 1997.

480 Hutchings, J. K. and Hibler III, W. D.: Small-scale sea ice deformation in the Beaufort Sea seasonal ice zone, Journal of Geophysical Research: Oceans, 113, https://doi.org/https://doi.org/10.1029/2006JC003971, https://agupubs.onlinelibrary.wiley.com/doi/abs/10.1029/2006JC003971, 2008.

Hutchings, J. K., Roberts, A., Geiger, C. A., and Richter-Menge, J.: Spatial and temporal characterization of sea-ice deformation, Annals of Glaciology, 52, 360–368, https://doi.org/10.3189/172756411795931769, 2011.

485 Hutchings, J. K., Heil, P., Steer, A., and Hibler III, W. D.: Subsynoptic scale spatial variability of sea ice deformation in the western Weddell Sea during early summer, Journal of Geophysical Research: Oceans, 117, https://doi.org/https://doi.org/10.1029/2011JC006961, https://agupubs.onlinelibrary.wiley.com/doi/abs/10.1029/2011JC006961, 2012.

Hutter, N., Bouchat, A., Dupont, F., Dukhovskoy, D., Koldunov, N., Lee, Y. J., Lemieux, J.-F., Lique, C., Losch, M., Maslowski, W., Myers, P. G., Ólason, E., Rampal, P., Rasmussen, T., Talandier, C., Tremblay, B., and Wang, Q.: Sea Ice Rheology Experi-490 ment (SIREx): 2. Evaluating Linear Kinematic Features in High-Resolution Sea Ice Simulations, Journal of Geophysical Research: Oceans, 127, e2021JC017 666, https://doi.org/https://doi.org/10.1029/2021JC017666, https://agupubs.onlinelibrary.wiley.com/doi/abs/10.1029/2021JC017666, e2021JC017666 2021JC017666, 2022.

16

Hwang, B. and Wang, Y.: Multi-scale satellite observations of Arctic sea ice: new insight into the life cycle of the floe size distribution, Philosophical Transactions of the Royal Society A: Mathematical, Physical and Engineering Sciences, 380, 20210 259, https://doi.org/10.1098/rsta.2021.0259, https://royalsocietypublishing.org/doi/abs/10.1098/rsta.2021.0259, 2022.

Itkin, P., Spreen, G., Hudson, S., Granskog, M., Gerland, S., Pavlov, A., et al.: N-ICE2015 buoy data [Data set], Norwegian Polar Institute, 10, https://doi.org/https://doi.org/10.21334/npolar.2015.6ed9a8ca, 2015.

Itkin, P., Spreen, G., Cheng, B., Doble, M., Girard-Ardhuin, F., Haapala, J., Hughes, N., Kaleschke, L., Nicolaus, M., and Wilkinson, J.: Thin ice and storms: Sea ice deformation from buoy arrays deployed during N-ICE2015, Journal of Geophysical Research: Oceans, 122, 4661–4674, https://doi.org/https://doi.org/10.1002/2016JC012403, https://agupubs.onlinelibrary.wiley.com/doi/abs/10.1002/2016JC012403, 2017.

Itkin, P., Spreen, G., Hvidegaard, S. M., Skourup, H., Wilkinson, J., Gerland, S., and Granskog, M. A.: Contribution of Deformation to Sea Ice Mass Balance: A Case Study From an N-ICE2015 Storm, Geophysical Research Letters, 45, 789–796, https://doi.org/https://doi.org/10.1002/2017GL076056, https://agupubs.onlinelibrary.wiley.com/doi/abs/10.1002/2017GL076056, 2018.

Karvonen, J.: Virtual radar ice buoys – a method for measuring fine-scale sea ice drift, The Cryosphere, 10, 29–42, https://doi.org/10.5194/tc-10-29-2016, https://tc.copernicus.org/articles/10/29/2016/, 2016.

Komarov, A. S. and Barber, D. G.: Sea Ice Motion Tracking From Sequential Dual-Polarization RADARSAT-2 Images, IEEE Transactions on Geoscience and Remote Sensing, 52, 121–136, https://doi.org/10.1109/TGRS.2012.2236845, 2014.

Korosov, A. A. and Rampal, P.: A Combination of Feature Tracking and Pattern Matching with Optimal Parametrization for Sea Ice Drift Retrieval from SAR Data, Remote Sensing, 9, https://doi.org/10.3390/rs9030258, https://www.mdpi.com/2072-4292/9/3/258, 2017.

Kwok, R.: The RADARSAT Geophysical Processor System, pp. 235–257, Springer Berlin Heidelberg, Berlin, Heidelberg, https://doi.org/10.1007/978-3-642-60282-5_11, https://doi.org/10.1007/978-3-642-60282-5_11, 1998.

Kwok, R. and Cunningham, G. F.: Variability of Arctic sea ice thickness and volume from CryoSat-2, Philosophical Transactions of the Royal Society A: Mathematical, Physical and Engineering Sciences, 373, 20140 157, https://doi.org/10.1098/rsta.2014.0157, https://royalsocietypublishing.org/doi/abs/10.1098/rsta.2014.0157, 2015.

Landy, J. C., Petty, A. A., Tsamados, M., and Stroeve, J. C.: Sea Ice Roughness Overlooked as a Key Source of Uncertainty in CryoSat-2 Ice Freeboard Retrievals, Journal of Geophysical Research: Oceans, 125, e2019JC015 820, https://doi.org/https://doi.org/10.1029/2019JC015820, https://agupubs.onlinelibrary.wiley.com/doi/abs/10.1029/2019JC015820, e2019JC015820 2019JC015820, 2020.

Liston, G. E., Itkin, P., Stroeve, J., Tschudi, M., Stewart, J. S., Pedersen, S. H., Reinking, A. K., and Elder, K.: A lagrangian snow-evolution system for sea-ice applications (SnowModel-LG): part I—model description, Journal of Geophysical Research: Oceans, 125, e2019JC015 913, https://doi.org/10.1029/2019JC015913, e2019JC015913 2019JC015913, 2020.

Lohse, J., Doulgeris, A. P., and Dierking, W.: Mapping sea-ice types from Sentinel-1 considering the surface-type dependent effect of incidence angle, Annals of Glaciology, 61, 260–270, https://doi.org/10.1017/aog.2020.45, 2020.

Marsan, D., Stern, H., Lindsay, R., and Weiss, J.: Scale Dependence and Localization of the Deformation of Arctic Sea Ice, Phys. Rev. Lett., 93, 178 501, https://doi.org/10.1103/PhysRevLett.93.178501, https://link.aps.org/doi/10.1103/PhysRevLett.93.178501, 2004.

Meredith, M., M. S. S. C. C. D. A. E. A. H. G. K. A. M. J. M.-T. M. M. G. O. H. P. and Schuur, E.: Polar Regions, IPCC Special Report on the Ocean and Cryosphere in a Changing Climate, pp. 203–320, https://doi.org/10.1017/9781009157964.005, https://doi.org/10.1017/9781009157964.005, 2019.

530 Murdza, A., Schulson, E. M., Renshaw, C. E., and Polojärvi, A.: Rapid Healing of Thermal Cracks in Ice, Geophysical Research Letters, 49, e2022GL099 771, https://doi.org/https://doi.org/10.1029/2022GL099771, https://agupubs.onlinelibrary.wiley.com/doi/abs/10.1029/2022GL099771, e2022GL099771 2022GL099771, 2022.

Nicolaus, M., Perovich, D. K., Spreen, G., Granskog, M. A., von Albedyll, L., Angelopoulos, M., Anhaus, P., Arndt, S., Belter, H. J., Bessonov, V., Birnbaum, G., Brauchle, J., Calmer, R., Cardellach, E., Cheng, B., Clemens-Sewall, D., Dadic, R., Damm, E., de Boer, G.,
535 Demir, O., Dethloff, K., Divine, D. V., Fong, A. A., Fons, S., Frey, M. M., Fuchs, N., Gabarró, C., Gerland, S., Goessling, H. F., Gradinger, R., Haapala, J., Haas, C., Hamilton, J., Hannula, H.-R., Hendricks, S., Herber, A., Heuzé, C., Hoppmann, M., Høyland, K. V., Huntemann, M., Hutchings, J. K., Hwang, B., Itkin, P., Jacobi, H.-W., Jaggi, M., Jutila, A., Kaleschke, L., Katlein, C., Kolabutin, N., Krampe, D., Kristensen, S. S., Krumpen, T., Kurtz, N., Lampert, A., Lange, B. A., Lei, R., Light, B., Linhardt, F., Liston, G. E., Loose, B., Macfarlane, A. R., Mahmud, M., Matero, I. O., Maus, S., Morgenstern, A., Naderpour, R., Nandan, V., Niubom, A., Oggier, M., Oppelt, N., Pätzold,
540 F., Perron, C., Petrovsky, T., Pirazzini, R., Polashenski, C., Rabe, B., Raphael, I. A., Regnery, J., Rex, M., Ricker, R., Riemann-Campe, K., Rinke, A., Rohde, J., Salganik, E., Scharien, R. K., Schiller, M., Schneebeli, M., Semmling, M., Shimanchuk, E., Shupe, M. D., Smith, M. M., Smolyanitsky, V., Sokolov, V., Stanton, T., Stroeve, J., Thielke, L., Timofeeva, A., Tonboe, R. T., Tavri, A., Tsamados, M., Wagner, D. N., Watkins, D., Webster, M., and Wendisch, M.: Overview of the MOSAiC expedition: snow and sea ice, Elementa: Science of the Anthropocene, 10, https://doi.org/10.1525/elementa.2021.000046, 000046, 2022.

545 Oikkonen, A., Haapala, J., Lensu, M., Karvonen, J., and Itkin, P.: Small-scale sea ice deformation during N-ICE2015: From compact pack ice to marginal ice zone, Journal of Geophysical Research: Oceans, 122, 5105–5120, https://doi.org/https://doi.org/10.1002/2016JC012387, https://agupubs.onlinelibrary.wiley.com/doi/abs/10.1002/2016JC012387, 2017.

Olason, E. and Notz, D.: Drivers of variability in Arctic sea-ice drift speed, Journal of Geophysical Research: Oceans, 119, 5755–5775, https://doi.org/https://doi.org/10.1002/2014JC009897, https://agupubs.onlinelibrary.wiley.com/doi/abs/10.1002/2014JC009897, 2014.

550 Parno, J., Polashenski, C., Parno, M., Nelsen, P., Mahoney, A., and Song, A.: Observations of Stress-Strain in Drifting Sea Ice at Floe Scale, Journal of Geophysical Research: Oceans, 127, e2021JC017 761, https://doi.org/https://doi.org/10.1029/2021JC017761, https://agupubs.onlinelibrary.wiley.com/doi/abs/10.1029/2021JC017761, e2021JC017761 2021JC017761, 2022.

Rampal, P., Weiss, J., and Marsan, D.: Positive trend in the mean speed and deformation rate of Arctic sea ice, 1979–2007, Journal of Geophysical Research: Oceans, 114, https://doi.org/https://doi.org/10.1029/2008JC005066, https://agupubs.onlinelibrary.wiley.com/doi/abs/10.1029/2008JC005066, 2009.
555

Rampal, P., Bouillon, S., Ólason, E., and Morlighem, M.: neXtSIM: a new Lagrangian sea ice model, The Cryosphere, 10, 1055–1073, https://doi.org/10.5194/tc-10-1055-2016, https://tc.copernicus.org/articles/10/1055/2016/, 2016.

Rampal, P., Dansereau, V., Olason, E., Bouillon, S., Williams, T., Korosov, A., and Samaké, A.: On the multi-fractal scaling properties of sea ice deformation, The Cryosphere, 13, 2457–2474, https://doi.org/10.5194/tc-13-2457-2019, https://tc.copernicus.org/articles/13/2457/
560 2019/, 2019.

Ricker, R., Hendricks, S., Kaleschke, L., Tian-Kunze, X., King, J., and Haas, C.: A weekly Arctic sea-ice thickness data record from merged CryoSat-2 and SMOS satellite data, The Cryosphere, 11, 1607–1623, https://doi.org/10.5194/tc-11-1607-2017, https://tc.copernicus.org/articles/11/1607/2017/, 2017.

Ringeisen, D., Hutter, N., and von Albedyll, L.: Deformation lines in Arctic sea ice: intersection angle distribution and mechanical properties,
565 The Cryosphere, 17, 4047–4061, https://doi.org/10.5194/tc-17-4047-2023, https://tc.copernicus.org/articles/17/4047/2023/, 2023.

Rösel, A., Itkin, P., King, J., Divine, D., Wang, C., Granskog, M. A., Krumpen, T., and Gerland, S.: Thin sea ice, thick snow, and widespread negative freeboard observed during N-ICE2015 north of Svalbard, Journal of Geophysical Research: Oceans, 123, 1156–1176, https://doi.org/10.1002/2017JC012865, 2018.

Salganik, E., Lange, B. A., Itkin, P., Divine, D., Katlein, C., Nicolaus, M., Hoppmann, M., Neckel, N., Ricker, R., Høyland, K. V., and Granskog, M. A.: Different mechanisms of Arctic first-year sea-ice ridge consolidation observed during the MOSAiC expedition, Elementa: Science of the Anthropocene, 11, 00 008, https://doi.org/10.1525/elementa.2023.00008, https://doi.org/10.1525/elementa.2023.00008, 2023.

Schulson, E. M.: Compressive shear faults within arctic sea ice: Fracture on scales large and small, Journal of Geophysical Research: Oceans, 109, https://doi.org/https://doi.org/10.1029/2003JC002108, https://agupubs.onlinelibrary.wiley.com/doi/abs/10.1029/2003JC002108, 2004.

Serreze, M. C. and Meier, W. N.: The Arctic's sea ice cover: trends, variability, predictability, and comparisons to the Antarctic, Annals of the New York Academy of Sciences, 1436, 36–53, https://doi.org/https://doi.org/10.1111/nyas.13856, https://nyaspubs.onlinelibrary.wiley.com/doi/abs/10.1111/nyas.13856, 2019.

Tian, T., Yang, S., Karami, M. P., Massonnet, F., Kruschke, T., and Koenigk, T.: Benefits of sea ice initialization for the interannual-to-decadal climate prediction skill in the Arctic in EC-Earth3, Geoscientific Model Development, 14, 4283–4305, https://doi.org/10.5194/gmd-14-4283-2021, https://gmd.copernicus.org/articles/14/4283/2021/, 2021.

von Albedyll, L., Haas, C., and Dierking, W.: Linking sea ice deformation to ice thickness redistribution using high-resolution satellite and airborne observations, The Cryosphere, 15, 2167–2186, https://doi.org/10.5194/tc-15-2167-2021, https://tc.copernicus.org/articles/15/2167/2021/, 2021.

von Albedyll, L., Hendricks, S., Grodofzig, R., Krumpen, T., Arndt, S., Belter, H. J., Birnbaum, G., Cheng, B., Hoppmann, M., Hutchings, J., Itkin, P., Lei, R., Nicolaus, M., Ricker, R., Rohde, J., Suhrhoff, M., Timofeeva, A., Watkins, D., Webster, M., and Haas, C.: Thermodynamic and dynamic contributions to seasonal Arctic sea ice thickness distributions from airborne observations, Elementa: Science of the Anthropocene, 10, 00 074, https://doi.org/10.1525/elementa.2021.00074, https://doi.org/10.1525/elementa.2021.00074, 2022.

Weiss, J.: Exploring the "solid turbulence" of sea ice dynamics down to unprecedented small scales, Journal of Geophysical Research: Oceans, 122, 6071–6075, https://doi.org/https://doi.org/10.1002/2017JC013236, https://agupubs.onlinelibrary.wiley.com/doi/abs/10.1002/2017JC013236, 2017.

Wernecke, A. and Kaleschke, L.: Lead detection in Arctic sea ice from CryoSat-2: quality assessment, lead area fraction and width distribution, The Cryosphere, 9, 1955–1968, https://doi.org/10.5194/tc-9-1955-2015, https://tc.copernicus.org/articles/9/1955/2015/, 2015.

Zakhvatkina, N., Smirnov, V., and Bychkova, I.: Satellite SAR Data-based Sea Ice Classification: An Overview, Geosciences, 9, https://doi.org/10.3390/geosciences9040152, https://www.mdpi.com/2076-3263/9/4/152, 2019.

Zygmuntowska, M., Rampal, P., Ivanova, N., and Smedsrud, L. H.: Uncertainties in Arctic sea ice thickness and volume: new estimates and implications for trends, The Cryosphere, 8, 705–720, https://doi.org/10.5194/tc-8-705-2014, 2014.

Ólason, E., Boutin, G., Korosov, A., Rampal, P., Williams, T., Kimmritz, M., Dansereau, V., and Samaké, A.: A New Brittle Rheology and Numerical Framework for Large-Scale Sea-Ice Models, Journal of Advances in Modeling Earth Systems, 14, e2021MS002 685, https://doi.org/https://doi.org/10.1029/2021MS002685, https://agupubs.onlinelibrary.wiley.com/doi/abs/10.1029/2021MS002685, e2021MS002685 2021MS002685, 2022.
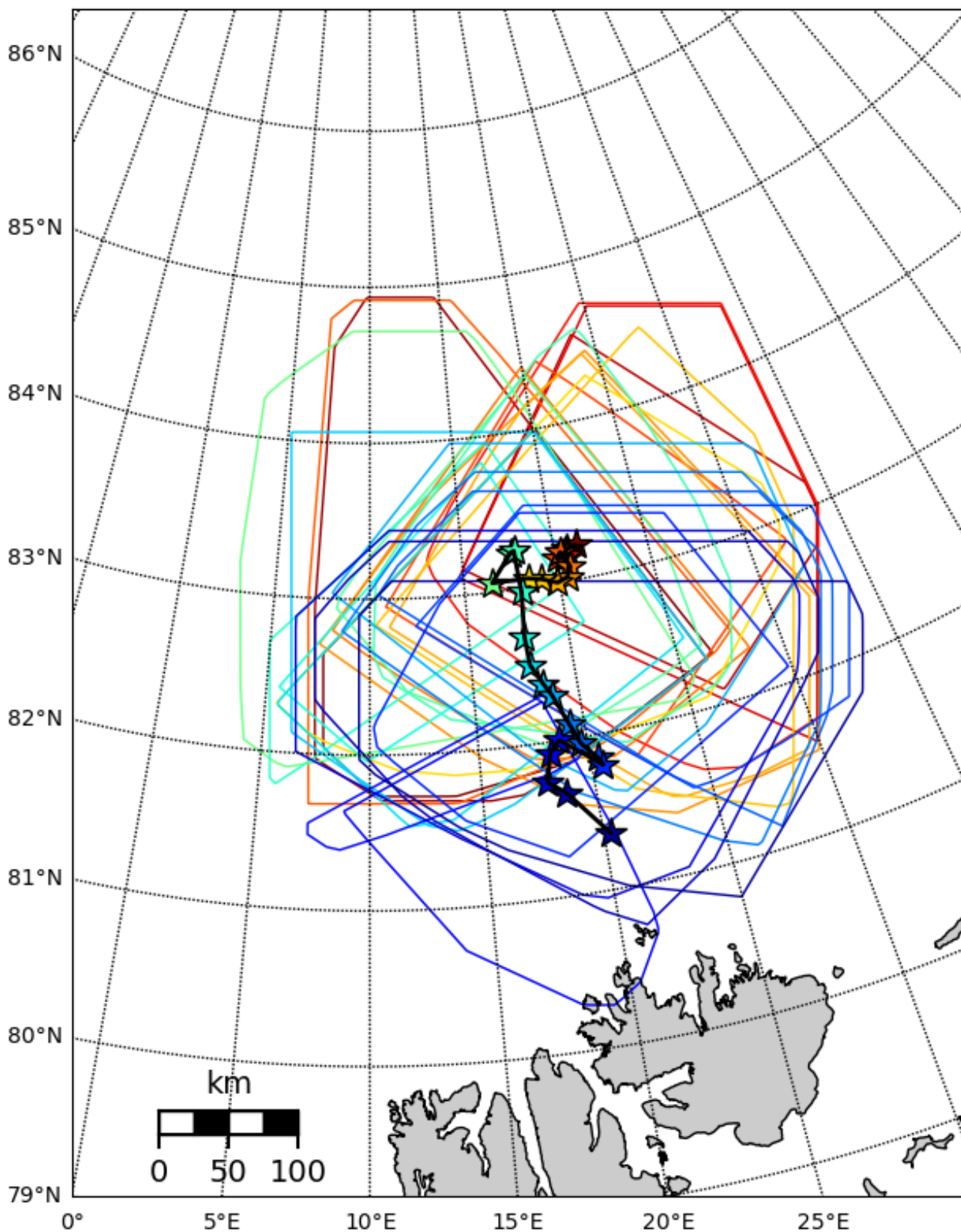
Figure 1. The N-ICE2015 RV Lance daily positions (stars) from 15 January to 18 February. The ship drifts southwards and colors of stars are increasing with time (jet colormap). The frames show total coverage of SAR sea ice deformation dataset for each day in the radius of 200km from RV Lance. By 27 February ship reached the ice edge and relocated back towards 83°N,25°E.
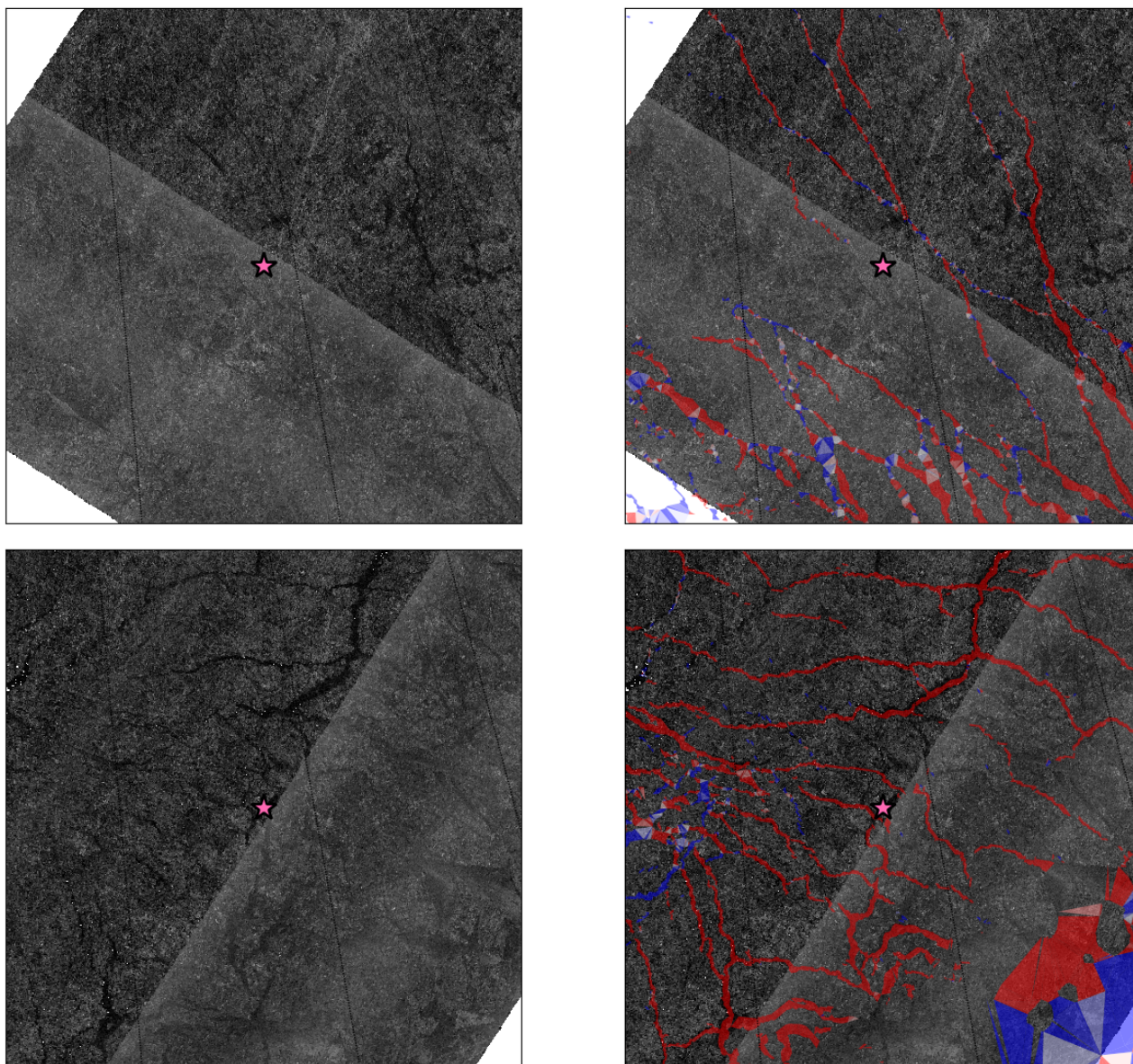
Figure 2. Second SAR image in the pair (left) overlaid by calculated deformation from the image pair (right) for 25 January (top) and 9 February 2015 (bottom). The sizes of the frames are 200km by 200 km. The location of RV Lance is represented by a pink star in the centers of the frames.
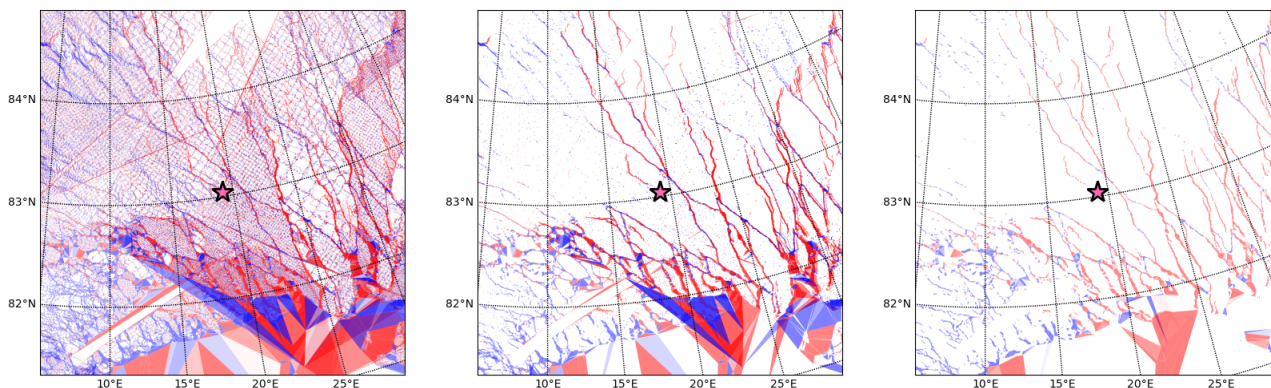
Figure 3. SAR deformation processing: original (left), DL filtered (center) and LKFF (right) for a mosaic of SAR image pairs for 25 January 2015. The sizes of the frames are 400km by 400 km. The location of RV Lance is represented by a pink star in the centers of the frames.
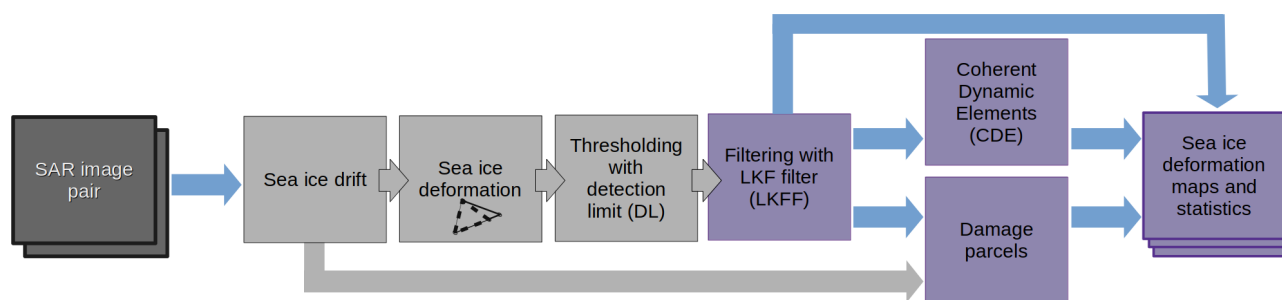
Figure 4. Flow chart of the SAR processing methods for sea ice deformation applied in this paper.
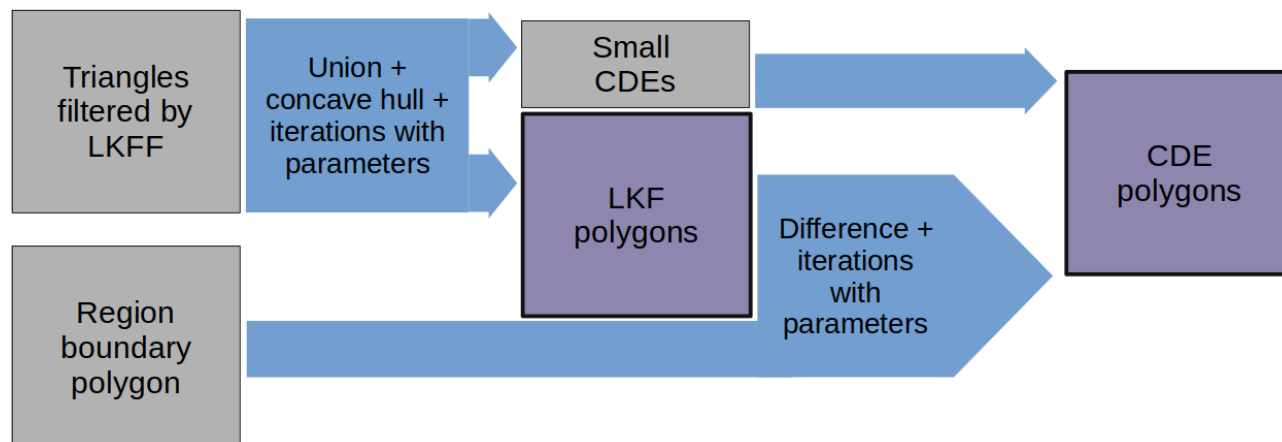
Figure 5. Flow chart of the CDE and LKF polygon operations. The vector operations are written on the blue arrows. Difference is a subtraction of intersection of two polygons.
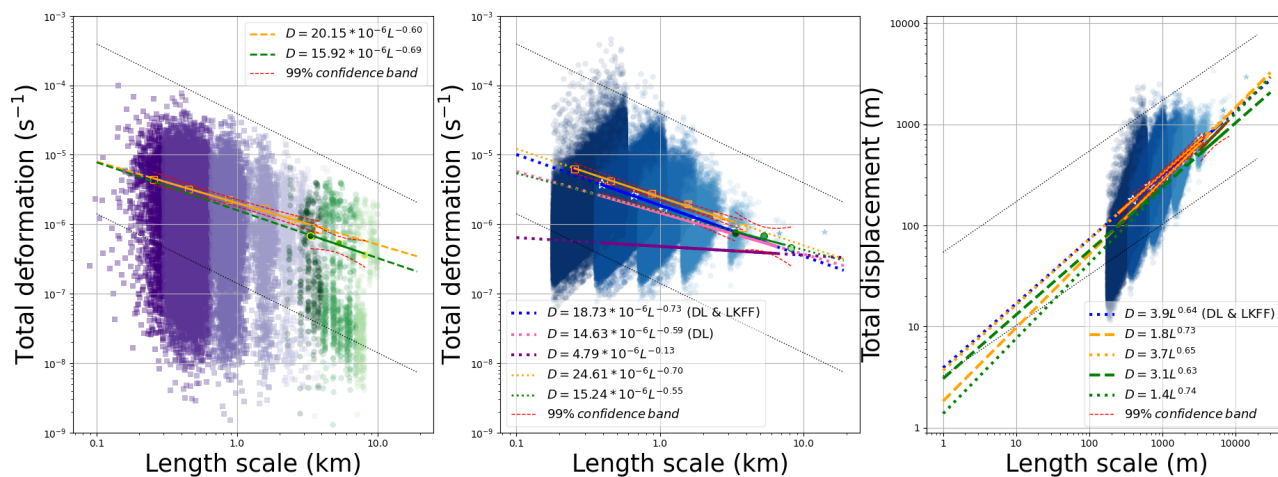
Figure 6. Power law for the spatial scales of ship radar-, buoy- and SAR-based sea ice deformation calculations: original values from ship radar and buoys (left), SAR-derived deformation and DL filtered ship radar and buoy values (center), and total displacements (right). Mean DL and max values are thin black dash lines on all plots.
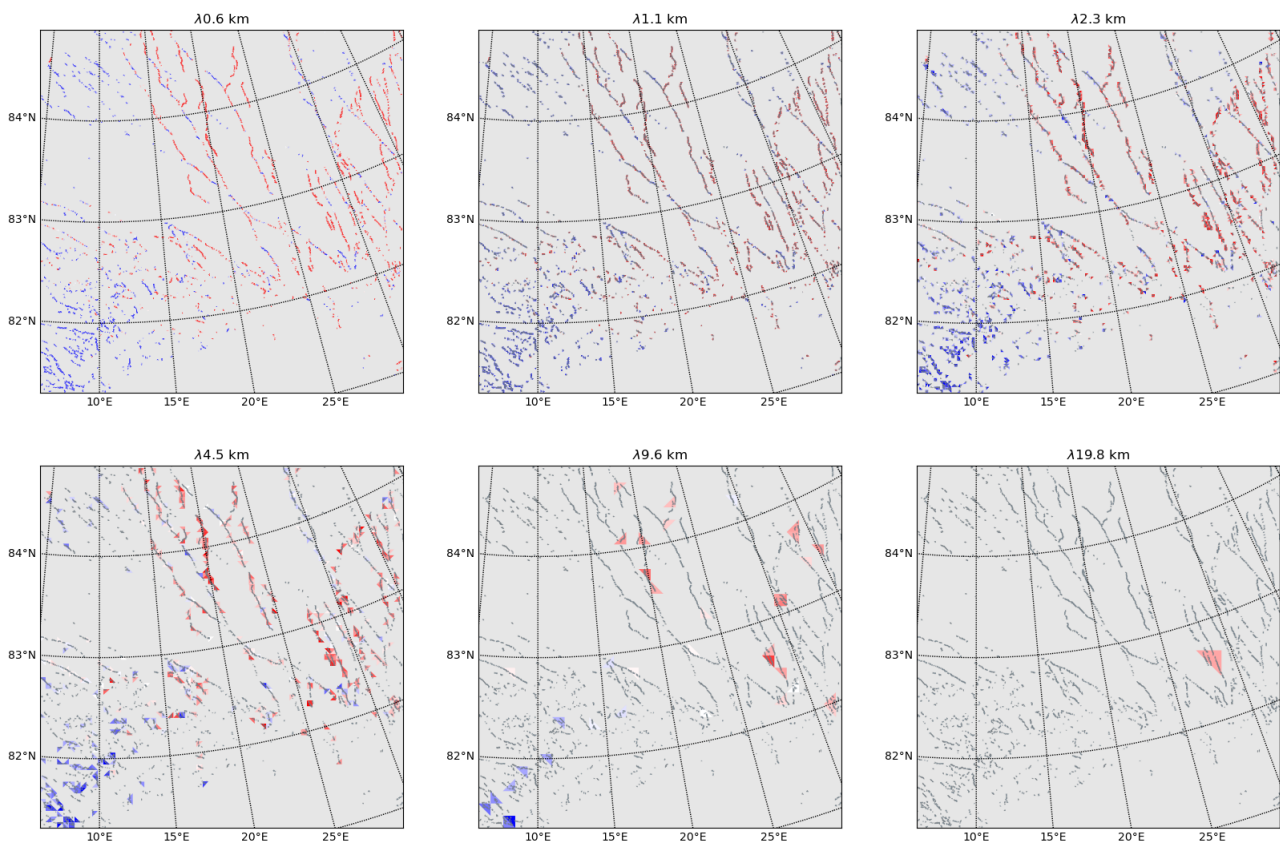
Figure 7. Example of coarse-graining of LKFF sea ice deformation for SAR image pairs for 25 January 2015. The sizes of the frames are 400km by 400 km. The area with values bellow DL is shaded in grey. The coverage of smallest triangles at λ 0.6 km is shown on all other panels with dark grey triangle outlines.
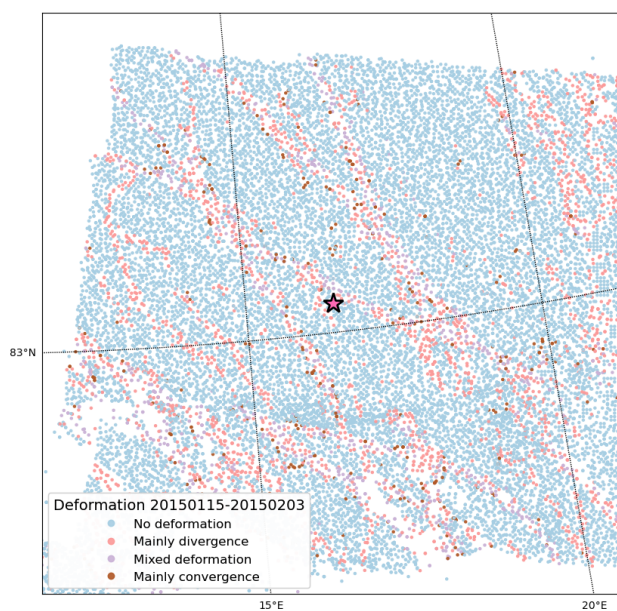
Figure 8. Damage parcel map after 19 days of sea ice drift between 15 January and 3 February 2015. The size of the map is 120 km by 120 km. The location of RV Lance is represented by a pink star in the center of the map.
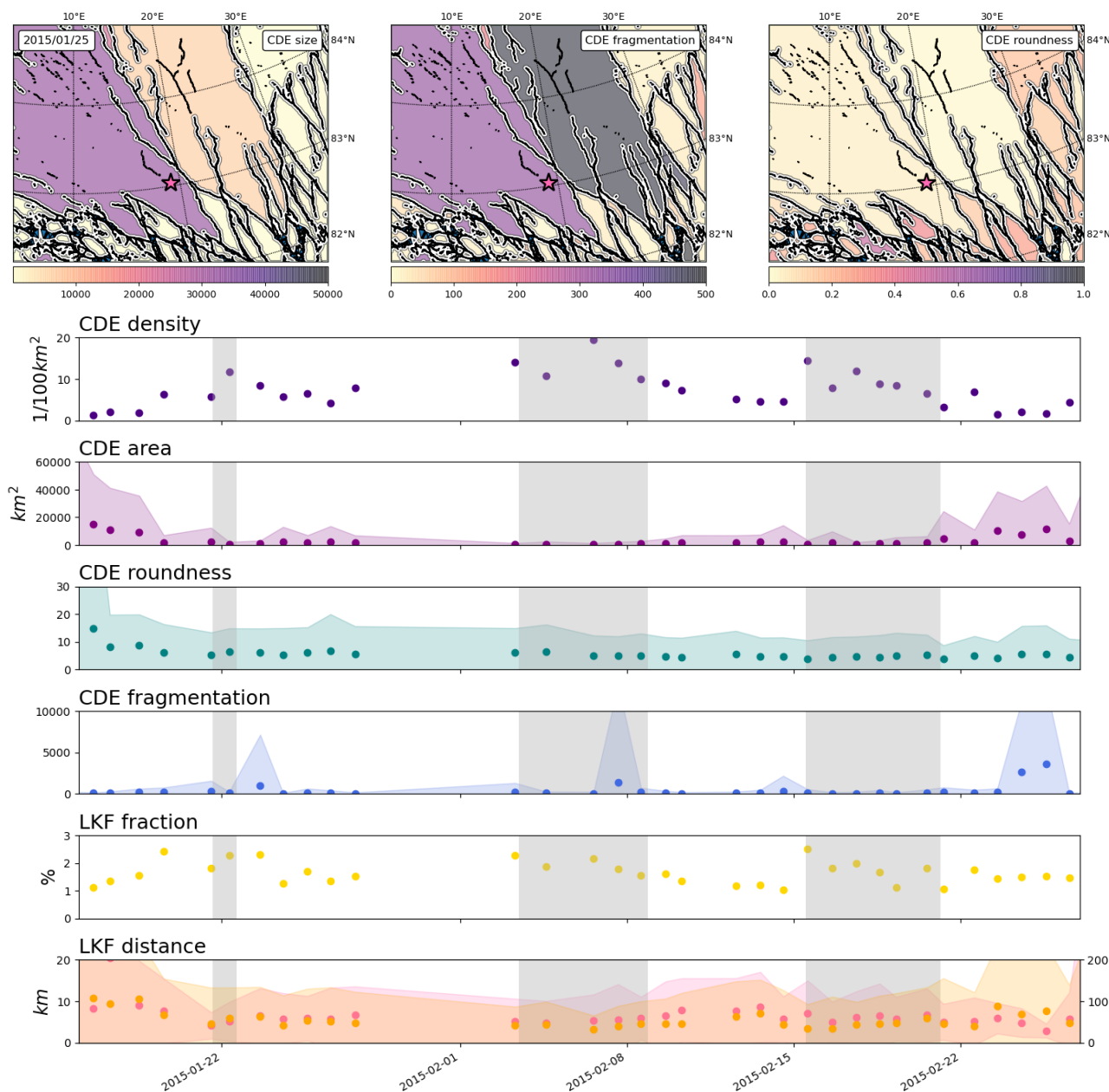
Figure 9. Top: Example of CDE maps with shape statistics for SAR image pairs for 25 January 2015. The sizes of the frames are 400km by 300 km. The location of RV Lance is represented by a pink star. The distance from ship to map edge is 100 km in the south and 200 km in other cardinal directions. This is to avoid including the open water area further south. Bottom: Time series of CDE statistics for N-ICE2015 leg 1 extended to 27 February 2015. In both case time stamps of the second image in the par is attributed to the result.